STScI | SPACE TELESCOPE SCIENCE INSTITUTE

TECHNICAL REPORT

Title: NIRISS Commissioning Results: NIS-020 – NIRISS Photometric Zeropoints (NGAS CAR-707, APT 1094)	Doc #: JWST-STScI-008267, SM-12 Date: 31October 2022 Rev: -
Authors: Paul Goudfrooij and the NIRISS team Phone: 410 338-4981	Release Date: 07 November 2022

1 Abstract

This report presents analysis and results of commissioning program NIS-020 (APT program 1094). We describe the data analysis used to measure NIRISS imaging throughput and compare the results with the pre-launch predictions by the JWST Exposure Time Calculator. We find throughputs that are 12-31% higher than those pre-launch predictions. The analysis described in this report is different from that in a separate report by Volk et al. (2022a), and serves as an independent check on the results. Our results are consistent with those of Volk et al., who focus more on the determination of the conversion factor between count rate and surface brightness in MJy/sr.

2 Introduction

Photometric throughputs were measured at two epochs for all available NIRISS imaging modes during commissioning, using APT program 1094. This includes direct imaging with all available NIRISS filters as well as NRM imaging with the filters supported for observations in the AMI mode. The results from this program also permit a relative photometric calibration between NIRISS and the other JWST instruments and will enable transformations between NIRISS and other photometric systems.

Targets were selected from the sample of Gordon et al. (2022) who assembled a list of 36 hot (white dwarf), A-type, and G-type flux standard stars for JWST calibration purposes. The faintest stars in this sample are faint enough to be imaged with small NIRISS subarrays with reasonable numbers of groups (samples) per integration without saturation. We chose white dwarf LDS 749B (K = 15.2, see Bohlin & Koester 2008) as our primary target. It was observed through all the direct imaging filters using the SUB128 and SUB256 subarrays, and a subset of filters using subarrays SUB64 and FULL in order to allow cross-calibration of the NIRISS subarrays. For the AMI observing mode, we observed the brighter flux standard P330-E (K = 11.4, a solar analog; see Bohlin & Landolt 2015) through all filters supported in the AMI mode, both in direct imaging and in NRM imaging mode. The data files and exposure specifications are listed in Table 1 below. All exposures used a 2-pt dither pattern with a step size of 4.5 pixels in X and Y. Numbers of groups and integrations per exposure were determined using the JWST ETC, and chosen to yield expected S/N ratios of 300 or greater.

The following analysis was performed on the `_cal.fits` data products from JWST calibration pipeline version 1.4.6, using CRDS context `jwst_0842.pmap`.

Table 1: Properties of exposures from APT program 1094 used for this analysis. The readout pattern was NISRAPID in all cases.

FITS file root ID	Target	Subarray	Pupil	Filter	Dithers	NGROUPS	NINTS
Observation 1*							
jw01094001001_02101	LDS 749B	SUB64	F115W	CLEAR	2	25	5
jw01094001001_02103	LDS 749B	SUB64	F150W	CLEAR	2	40	5
jw01094001001_02105	LDS 749B	SUB64	F200W	CLEAR	2	75	5
jw01094001001_02107	LDS 749B	SUB128	F200W	CLEAR	2	20	3
jw01094001001_02109	LDS 749B	SUB128	F150W	CLEAR	2	10	3
jw01094001001_0210b	LDS 749B	SUB128	F140M	CLEAR	2	20	3
jw01094001001_0210d	LDS 749B	SUB128	F158M	CLEAR	2	25	3
jw01094001001_0210f	LDS 749B	SUB128	F115W	CLEAR	2	7	3
jw01094001001_0210h	LDS 749B	SUB128	F090W	CLEAR	2	7	3
jw01094001001_0210j	LDS 749B	SUB128	CLEARP	F480M	2	800	5
jw01094001001_0210l	LDS 749B	SUB128	CLEARP	F380M	2	800	3
jw01094001001_0210n	LDS 749B	SUB128	CLEARP	F430M	2	800	4
jw01094001001_0210p	LDS 749B	SUB128	CLEARP	F356W	2	180	3
jw01094001001_0210r	LDS 749B	SUB128	CLEARP	F444W	2	340	3
jw01094001001_0210t	LDS 749B	SUB128	CLEARP	F277W	2	80	3
jw01094001001_0210v	LDS 749B	SUB256	CLEARP	F277W	2	20	3
jw01094001001_0210x	LDS 749B	SUB256	CLEARP	F444W	2	90	3
jw01094001001_0210z	LDS 749B	SUB256	CLEARP	F356W	2	40	3
jw01094001001_02111	LDS 749B	SUB256	CLEARP	F430M	2	350	3
jw01094001001_02113	LDS 749B	SUB256	CLEARP	F380M	2	245	3
jw01094001001_02115	LDS 749B	SUB256	CLEARP	F480M	2	400	3
jw01094001001_02117	LDS 749B	SUB256	F200W	CLEAR	2	6	3
jw01094001001_02119	LDS 749B	SUB256	F150W	CLEAR	2	4	3
jw01094001001_0211b	LDS 749B	SUB256	F140M	CLEAR	2	6	3
jw01094001001_0211d	LDS 749B	SUB256	F158M	CLEAR	2	7	3
jw01094001001_0211f	LDS 749B	SUB256	F115W	CLEAR	2	3	3
jw01094001001_0211h	LDS 749B	SUB256	F090W	CLEAR	2	2	4
jw01094001002_02101	LDS 749B	FULL	CLEARP	F444W	2	5	3
jw01094001002_02103	LDS 749B	FULL	CLEARP	F356W	2	3	3
jw01094001002_02105	LDS 749B	FULL	CLEARP	F430M	2	20	3
jw01094001002_02107	LDS 749B	FULL	CLEARP	F380M	2	10	3
jw01094001002_02109	LDS 749B	FULL	CLEARP	F480M	2	25	3
Observation 2*							
jw01094002001_03102	P330-E	SUB80	CLEARP	F480M	2	100	3
jw01094002001_03104	P330-E	SUB80	CLEARP	F380M	2	35	3
jw01094002001_03106	P330-E	SUB80	CLEARP	F430M	2	70	3
jw01094002001_03108	P330-E	SUB80	CLEARP	F277W	2	3	3
jw01094002001_0310a	P330-E	SUB80	NRM	F430M	2	800	5
jw01094002001_0310c	P330-E	SUB80	NRM	F380M	2	800	3
jw01094002001_0310e	P330-E	SUB80	NRM	F480M	2	800	9
jw01094002001_0310g	P330-E	FULL	NRM	F480M	2	20	2

*** All exposures in Observation 1 and 2 were taken on May 21, 2022, and re-observed in Observation 3 and 4, respectively, for a second epoch on June 6, 2022.**

3 Aperture Photometry

Aperture photometry was performed using scripts in the `nis_comm/nis_020_alternate` folder of the NIRISS Commissioning repository on GitHub (https://github.com/spacetelescope/niriss-commissioning). The main function used here is `pgphotdefs.pgphotdit2` along with wrapper scripts that manage output file names and the aperture radii for the measurements. The main steps performed can be summarized as follows:

1. Read in the `_cal.fits` files, then divide the science extensions by the value of header keyword PHOTMJSR so as to obtain flat-fielded count rate images in units of ADU/s.
2. Establish high-precision center positions for the target star in the two dither positions. This is done by using 2-D Gaussian fits (`photutils.centroids.centroid_2dg`), which method was recently shown to provide the most robust and precise centroids for undersampled NIRISS PSFs (Goudfrooij 2022). The estimated position of the star in the first dither was the SIAF aperture position associated with the subarray used for the exposure (see Goudfrooij & Cox 2017), and the estimated star position for the second dither was calculated from the XOFFSET and YOFFSET header keywords translated to positions in the "science" (DMS) coordinate frame using script `idealdithers.py`.
3. Determine a clipped mean background level for each image and subtract it, so as to obtain 2 dithered images (per filter) with the same (zero) background level.
4. Using the DQ arrays, identify bad (though not saturated) pixels around the target in each image using X and Y positions relative to that of the location of the target. If a pixel is bad in only one of the two dithers, replace its value by that in the other dither (using that target-centered coordinate system). If a pixel is bad in both dithers, replace it by means of 2-D interpolation using its neighbors. (Note: This step is only done outside a radius of 3 pixels.)
5. For each of the two images, use κ-σ clipping statistics in the sky measurement region to determine the signal threshold below which (anomalously low) sky values be clipped out of the range used to calculate statistics on the sky level. This step turned out to be especially important for data taken with the SUB128 subarray, for which several pixels with significantly negative values are present around the source regions in the case of short exposures such as those taken with the short-wavelength filters (see Figure 1).
6. Add the background levels found in step 3 above back into the images.
7. Perform multi-aperture photometry using `photutils.aperture_photometry`. For the purpose of these measurements, we used aperture radii of 1-15 pixels with a step of 1 pixel for all subarrays. For the subarrays larger than SUB64 (i.e., SUB80, SUB128, SUB256, and FULL), we appended more measurement radii to get useful encircled energy measurements. This was done in steps of 5 pixels (out to a maximum of 60 pixels), while making sure to never reach the edge of the subarray in question with the outermost measurement radii. Sky levels and their errors were determined as the clipped mean and standard deviation in a 5-pixel wide annulus with an inner radius starting 10 pixels outside the outermost object measurement radius.
8. Calculate object and sky counts in electrons per integration in order to calculate proper photometric errors, and calculate fluxes and their errors in units of electrons/s. We assume a gain of 1.61 electrons/ADU for the NIRISS detector in this step.
9. Combine the measurements from the two dithers into one file per filter, and calculate

weighted average fluxes.

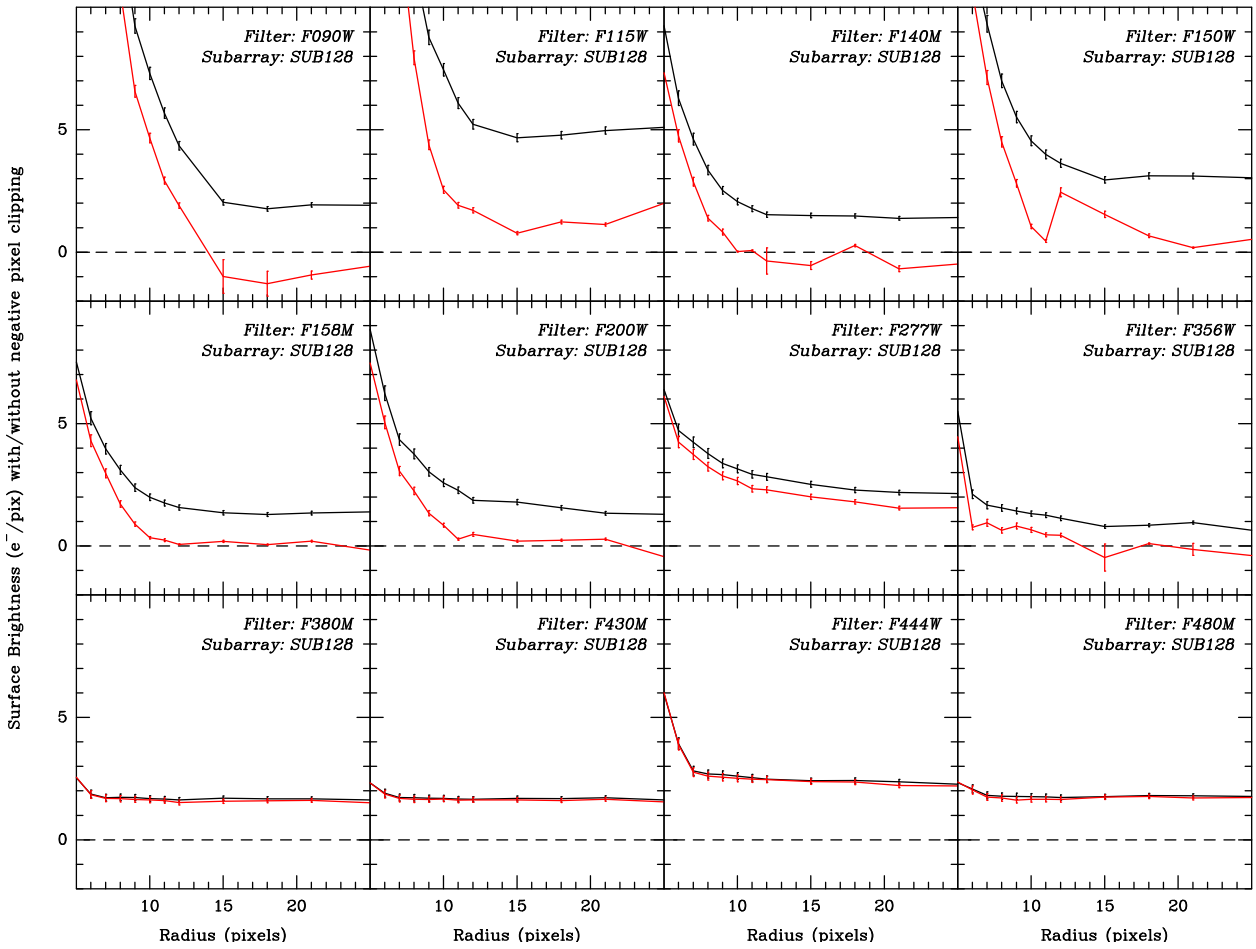

Figure 1: azimuth-averaged surface brightness as function of radius from the star centroid for the SUB128 images of Observation 1. Sky background has not been subtracted. Red symbols and lines represent measurements made without κ-σ clipping statistics to eliminate anomalously low pixel values, while black symbols and lines represent measurements that do use κ-σ clipping. See text in enumerated item #5 in §3.

For the determination of aperture corrections, we also created images using `WebbPSF` (Perrin et al. 2012, 2014) for each filter and dither position, using the exact same center positions as those found for the observed star, an oversampling factor of 11, and a size of 301×301 pixels with the native NIRISS pixel size. This step is done using script `mkwebbPSFs.py`, using the star centroids in the output files from step 7 above as input. Note that `WebbPSF` output images are normalized to an integrated flux of unity at the exit pupil in the process. We then repeated steps 2 and 7-9 above for those PSF images to obtain the aperture corrections, making sure that the fractions of the PSF's source flux in the sky annulus are also accounted for.

The aperture corrections were applied to the aperture photometry of the flux standard stars using script `EEnormalize_nis.py` (where EE stands for encircled energy), which applies the aperture correction by multiplying the observed fluxes by the average ratio "EE (PSF) / EE (star)" for a given filter within a specified range of aperture radii. After some experimentation, we chose a

range in radius from 8 to 12 pixels for this purpose for the case of "normal" direct imaging (with filters in the pupil wheel or filters in the filter wheel plus the CLEARP element in the pupil wheel) and 12 to 15 pixels for imaging with the NRM. These radii are large enough to avoid the dependency on precise centering of undersampled PSFs relative to pixel borders; the impact of these dependencies can be significant at small radii (this will be discussed and quantified in detail in a separate report). The outer object measurement radius of 12 pixels (or 15 pixels for the NRM) also avoids the region with relatively large photometric uncertainties due to the low surface brightness of the star at those large radii. EEs for the various direct imaging and NRM imaging modes for NIS-20 data are shown in Figures 2 and 3.

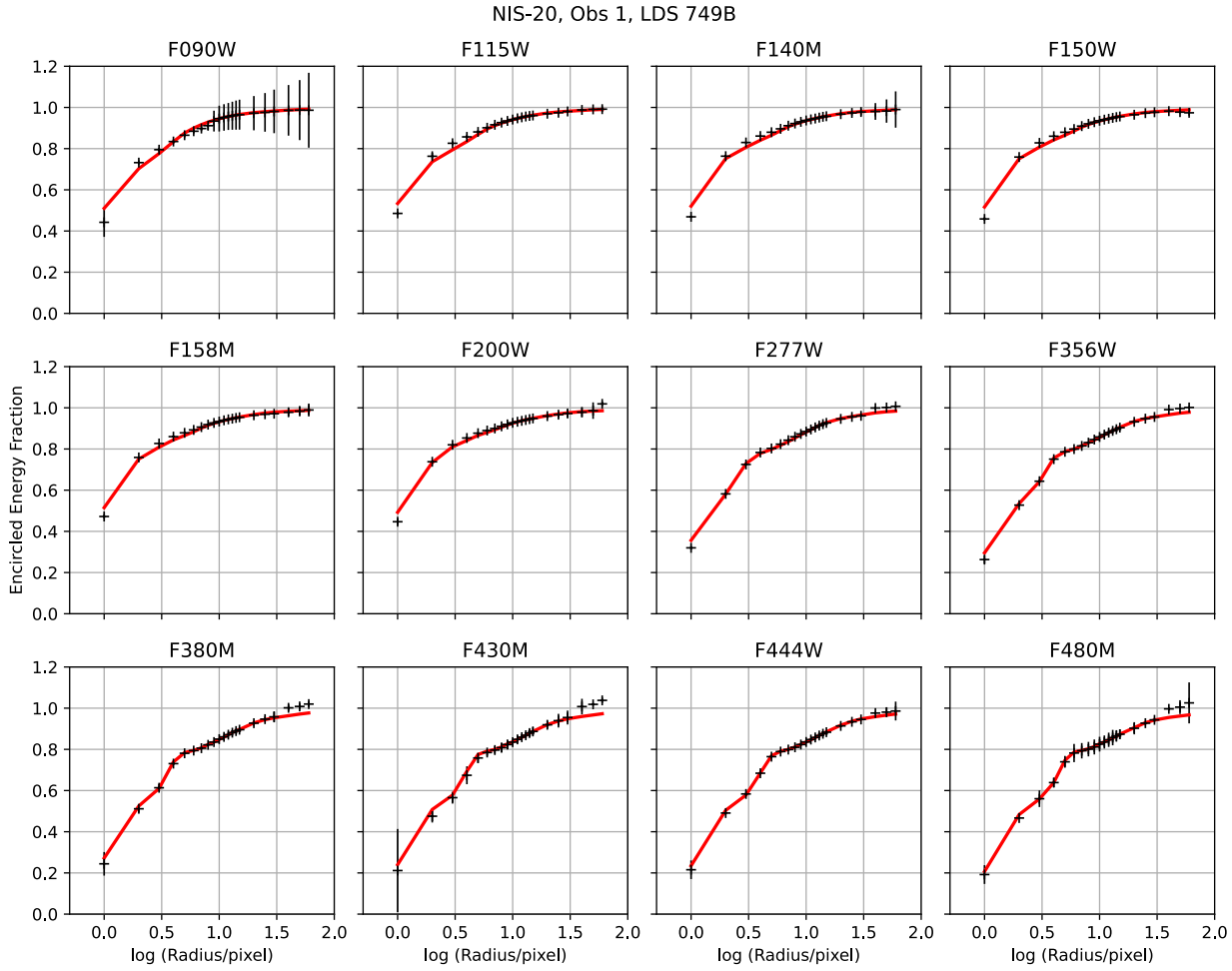

Figure 2: encircled energy curves from direct imaging data of NIS-20. Filters are shown at the top of each panel. Data points with error bars represent average aperture photometry of LDS 749B from Observation 1 using the SUB256 subarray, normalized by the aperture photometry of the WebbPSF images placed at the same positions as the star. The WebbPSF photometry is shown as a red line in each panel.

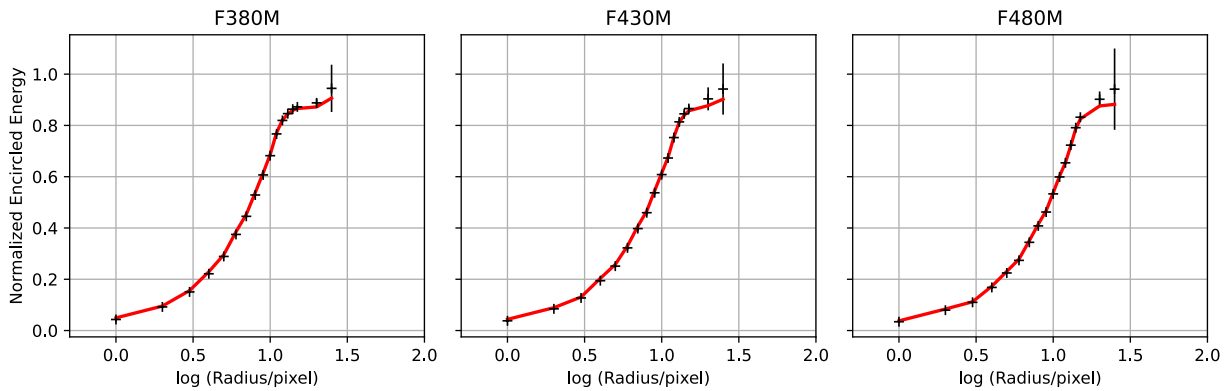

Figure 3: similar to Figure 2, but now for NRM imaging data of NIS-20. Data points now represent aperture photometry of P330-E from Observation 2 using the SUB80 subarray.

4 Results

Tables 2-6 list the measured integrated count rates for LDS 749B and P330-E and compare them with predictions based on the ETC reference files on observatory and instrument throughput which represent estimates from pre-launch measurements (see Pontoppidan et al. 2015). Two such predictions are provided:

1. Predictions straight from the ETC, which uses `WebbPSF` PSFs for aperture photometry. For this purpose, we use a measurement radius of 3.936 arcsec, corresponding to 60 NIRISS pixels, and correct the resulting count rates using the aperture correction for that measurement radius derived in the preceding section. For the source spectra, we uploaded the CALSPEC spectra `lds749b_mod_006.fits` and `p330e_mod_004.fits` for LDS749B and P330E, respectively, onto the ETC for this purpose.
2. Predictions from a NIRISS throughput model based on the `synphot (or pysynphot)` package, with throughput files made available in `/ifs/jwst/wit/niriss/synphot`, using the same CALSPEC spectra as input. We adopt a primary mirror area of 254009.0 cm^2 for JWST, as used in the `Pandeia` engine of the (pre-launch) JWST ETC. We use scripts `NIRISScountrates.py` and `NIRISScountrates_nrm.py` for these predictions. We denote these predictions as the "NIRISS model" predictions in the remainder of this report.

Relevant results from the photometry are illustrated in Figures 2-9 and described below.

Table 2: Integrated, aperture-corrected count rates for flux standard star LDS 749B using subarray SUB64. Results from observation 1 are shown in black while those from observation 3 are shown in blue.

Pupil	Filter	Count Rate	Prediction (NIRISS model)	Predicted (ETC)	Obs/Model ratio	Obs/ETC ratio
F115W	CLEAR	128298 ± 7846	1.138e+05	1.083e+05	1.127 ± 0.069	1.185 ± 0.072
		126865 ± 6510			1.115 ± 0.007	1.171 ± 0.060
F150W	CLEAR	73276 ± 1249	6.594e+04	6.224e+04	1.111 ± 0.019	1.177 ± 0.020
		72403 ± 438			1.098 ± 0.007	1.163 ± 0.007
F200W	CLEAR	41183 ± 3427	4.327e+04	4.057e+04	0.952 ± 0.079	1.015 ± 0.084
		40900 ± 3257			0.945 ± 0.075	1.008 ± 0.080

Table 3: like Table 2, but now for subarray SUB128

Pupil	Filter	Count Rate	Prediction (NIRISS model)	Predicted (ETC)	Obs/Model ratio	Obs/ETC ratio
F090W	CLEAR	180075 ± 373	1.515e+05	1.452e+05	1.189 ± 0.002	1.240 ± 0.003
		178933 ± 1838			1.181 ± 0.012	1.232 ± 0.013
F115W	CLEAR	132783 ± 3101	1.138e+05	1.083e+05	1.167 ± 0.027	1.226 ± 0.029
		132368 ± 2004			1.163 ± 0.018	1.222 ± 0.019
F140M	CLEAR	43333 ± 127	3.493e+04	3.308e+04	1.241 ± 0.004	1.310 ± 0.004
		43554 ± 1172			1.247 ± 0.034	1.316 ± 0.010
F150W	CLEAR	79634 ± 208	6.597e+04	6.224e+04	1.207 ± 0.003	1.279 ± 0.003
		81641 ± 601			1.238 ± 0.009	1.312 ± 0.010
F158M	CLEAR	36190 ± 89	3.075e+04	2.836e+04	1.177 ± 0.003	1.276 ± 0.003
		35972 ± 297			1.170 ± 0.010	1.268 ± 0.010
F200W	CLEAR	46269 ± 404	4.327e+04	4.057e+04	1.069 ± 0.009	1.141 ± 0.010
		46063 ± 558			1.065 ± 0.013	1.135 ± 0.014
CLEARP	F277W	26819 ± 43	2.456e+04	2.207e+04	1.092 ± 0.002	1.215 ± 0.002
		26679 ± 64			1.086 ± 0.003	1.209 ± 0.003
CLEARP	F356W	17341 ± 35	1.579e+03	1.395e+03	1.098 ± 0.002	1.243 ± 0.002
		17311 ± 29			1.090 ± 0.002	1.233 ± 0.002
CLEARP	F380M	3139 ± 10	2.855e+03	2.747e+03	1.099 ± 0.003	1.267 ± 0.004
		3137 ± 29			1.099 ± 0.010	1.266 ± 0.012
CLEARP	F430M	1952 ± 9	1.833e+03	1.589e+03	1.065 ± 0.005	1.228 ± 0.006
		1927 ± 19			1.051 ± 0.010	1.213 ± 0.012
CLEARP	F444W	10733 ± 49	9.589e+03	8.322e+03	1.119 ± 0.005	1.290 ± 0.006
		10681 ± 21			1.114 ± 0.002	1.283 ± 0.002
CLEARP	F480M	1799 ± 15	1.636e+03	1.391e+03	1.100 ± 0.009	1.293 ± 0.011
		1793 ± 23			1.096 ± 0.014	1.288 ± 0.016

Table 4: like Table 2, but now for subarray SUB256

Pupil	Filter	Count Rate	Prediction (NIRISS model)	Predicted (ETC)	Obs/Model ratio	Obs/ETC ratio
F090W	CLEAR	185481 ± 11602	1.515e+05	1.452e+05	1.224 ± 0.077	1.277 ± 0.080
		179991 ± 396			1.188 ± 0.003	1.239 ± 0.003
F115W	CLEAR	137195 ± 1021	1.138e+05	1.083e+05	1.206 ± 0.009	1.267 ± 0.009
		134005 ± 5248			1.178 ± 0.046	1.237 ± 0.048
F140M	CLEAR	43289 ± 100	3.493e+04	3.308e+04	1.239 ± 0.003	1.308 ± 0.003
		43044 ± 131			1.232 ± 0.004	1.301 ± 0.004
F150W	CLEAR	80394 ± 209	6.597e+04	6.224e+04	1.223 ± 0.003	1.296 ± 0.003
		79825 ± 536			1.210 ± 0.008	1.282 ± 0.009
F158M	CLEAR	36327 ± 135	3.075e+04	2.836e+04	1.181 ± 0.004	1.281 ± 0.005
		36020 ± 97			1.168 ± 0.003	1.267 ± 0.003
F200W	CLEAR	46363 ± 195	4.327e+04	4.057e+04	1.071 ± 0.005	1.143 ± 0.015
		46117 ± 210			1.066 ± 0.005	1.137 ± 0.005
CLEARP	F277W	27220 ± 77	2.456e+04	2.207e+04	1.108 ± 0.003	1.234 ± 0.004
		27028 ± 150			1.100 ± 0.006	1.225 ± 0.007
CLEARP	F356W	17512 ± 32	1.579e+03	1.395e+03	1.109 ± 0.002	1.255 ± 0.002
		17473 ± 35			1.100 ± 0.002	1.245 ± 0.002
CLEARP	F380M	3135 ± 5	2.855e+03	2.747e+03	1.098 ± 0.002	1.266 ± 0.002
		3124 ± 21			1.094 ± 0.007	1.261 ± 0.008

Pupil	Filter	Count Rate	Prediction (NIRISS model)	Predicted (ETC)	Obs/Model ratio	Obs/ETC ratio
CLEARP	F430M	1952 ± 5	1.833e+03	1.589e+03	1.065 ± 0.003	1.228 ± 0.003
		1930 ± 12			1.053 ± 0.007	1.214 ± 0.008
CLEARP	F444W	10802 ± 14	9.589e+03	8.322e+03	1.126 ± 0.001	1.298 ± 0.002
		10719 ± 44			1.118 ± 0.005	1.288 ± 0.005
CLEARP	F480M	1784 ± 9	1.636e+03	1.391e+03	1.091 ± 0.005	1.282 ± 0.006
		1770 ± 3			1.082 ± 0.002	1.272 ± 0.002

Table 5: like Table 2, but now for subarray FULL

Pupil	Filter	Count Rate	Prediction (NIRISS model)	Predicted (ETC)	Obs/Model ratio	Obs/ETC ratio
CLEARP	F356W	17223 ± 939	1.579e+03	1.395e+03	1.091 ± 0.059	1.234 ± 0.067
		16961 ± 898			1.074 ± 0.057	1.216 ± 0.064
CLEARP	F380M	3191 ± 14	2.855e+03	2.747e+03	1.118 ± 0.005	1.288 ± 0.006
		3126 ± 60			1.095 ± 0.021	1.262 ± 0.024
CLEARP	F430M	1937 ± 87	1.833e+03	1.589e+03	1.056 ± 0.048	1.218 ± 0.055
		1976 ± 18			1.078 ± 0.010	1.244 ± 0.011
CLEARP	F444W	10785 ± 513	9.589e+03	8.322e+03	1.125 ± 0.053	1.296 ± 0.062
		10728 ± 447			1.119 ± 0.047	1.289 ± 0.054
CLEARP	F480M	1778 ± 72	1.636e+03	1.391e+03	1.087 ± 0.044	1.278 ± 0.052
		1780 ± 11			1.099 ± 0.007	1.292 ± 0.008

Table 6: Integrated, aperture-corrected count rates for flux standard star P330-E using subarray SUB80. Results from observation 2 are shown in black while those from observation 4 are shown in blue.

Pupil	Filter	Count Rate	Prediction (NIRISS model)	Predicted (ETC)	Obs/Model ratio	Obs/ETC ratio
CLEARP	F277W	796356 ± 8588	6.825e+05	6.528e+05	1.167 ± 0.013	1.220 ± 0.013
		786858 ± 7380			1.089 ± 0.010	1.205 ± 0.011
CLEARP	F380M	97334 ± 779	8.164e+04	7.551e+04	1.192 ± 0.010	1.289 ± 0.010
		95842 ± 221			1.152 ± 0.003	1.269 ± 0.003
CLEARP	F430M	59839 ± 501	5.302e+04	4.875e+04	1.129 ± 0.009	1.227 ± 0.010
		59338 ± 761			1.107 ± 0.014	1.217 ± 0.016
CLEARP	F480M	53949 ± 1081	4.692e+04	4.244e+04	1.150 ± 0.023	1.271 ± 0.025
		53951 ± 617			1.150 ± 0.013	1.271 ± 0.015
NRM	F380M	16799 ± 33	1.458e+04	1.669e+04	1.152 ± 0.002	1.187 ± 0.002
		16695 ± 70			1.145 ± 0.005	1.180 ± 0.005
NRM	F430M	10652 ± 47	9.469e+03	9.074e+03	1.125 ± 0.005	1.174 ± 0.005
		10576 ± 72			1.117 ± 0.008	1.166 ± 0.008
NRM	F480M	9341 ± 124	8.379e+03	7.900e+03	1.115 ± 0.015	1.182 ± 0.016
		9390 ± 23			1.121 ± 0.003	1.189 ± 0.003

4.1 Issue with frame read time for SUB64 subarray

Figures 4 and 5 show the measured signal levels of LDS 749B through all NIRISS filters taken with different subarrays, relative to the predictions of the NIRISS model and the ETC, for the two different observing epochs. It can be seen that the data taken using the SUB128, SUB256, and FULL subarrays are consistent with one another to within the uncertainties (as expected), while the signal levels measured using the SUB64 subarray are systematically lower, although the relatively large uncertainties of the SUB64 photometry formally render this to be statistically

significant only for the F158M filter. Quantitatively, we find an inverse-variance-weighted mean ratio SUB64/((SUB128+SUB256)/2) = 0.914 ± 0.016. In investigating possible causes of this issue, one option being considered was that the frame read time for the SUB64 subarray was somehow defined incorrectly in the relevant on-board operation script of OSS (Operations Scripts Subsystem) and in the NIRISS Subarray properties file in the OPSSOC PRD. The frame read times in those files were calculated according to the frame read time formulae for instruments other than FGS in the official ASIC SIDECAR Interface Requirements and Control Document (JWST-IRCD-004971 Rev. H, Lander et al. 2018, pages 4-68 through 4-70). Further investigation by Eddie Bergeron and Julia Zhou uncovered that for NIRISS, subarrays with size 64×64 or smaller were actually read out using the "FGS" configuration, which uses shorter overheads than for the other instruments with H2RG detectors. This means that the frame read time for SUB64 is actually 0.04550 s rather than the assumed value of 0.05016 s. The ratio of these frame read times is 0.907, which is equal to the observed ratio mentioned above to within 1σ. As such, we assumed that the observed discrepancy was simply due to the erroneous frame time in the FITS header for NIRISS subarrays with 64×64 pixels (i.e., subarrays SUB64, SUBTAAMI, and SUBTASOSS). The OSS script that defines the frame read times for subarrays (the NISDEFSUB script) was corrected and uploaded to the telescope as part of OSS Build 8.4.9, and the NIRISS subarray properties file in the OPSSOC PRD was updated as part of version PRDOPSSOC-054 (released on June 21, 2022). The latter ensured that data taken with the subarrays with 64×64 pixels since that date get the correct frame time in their FITS header keyword TFRAME which will ensure a correct count rate calculation during pipeline calibration.

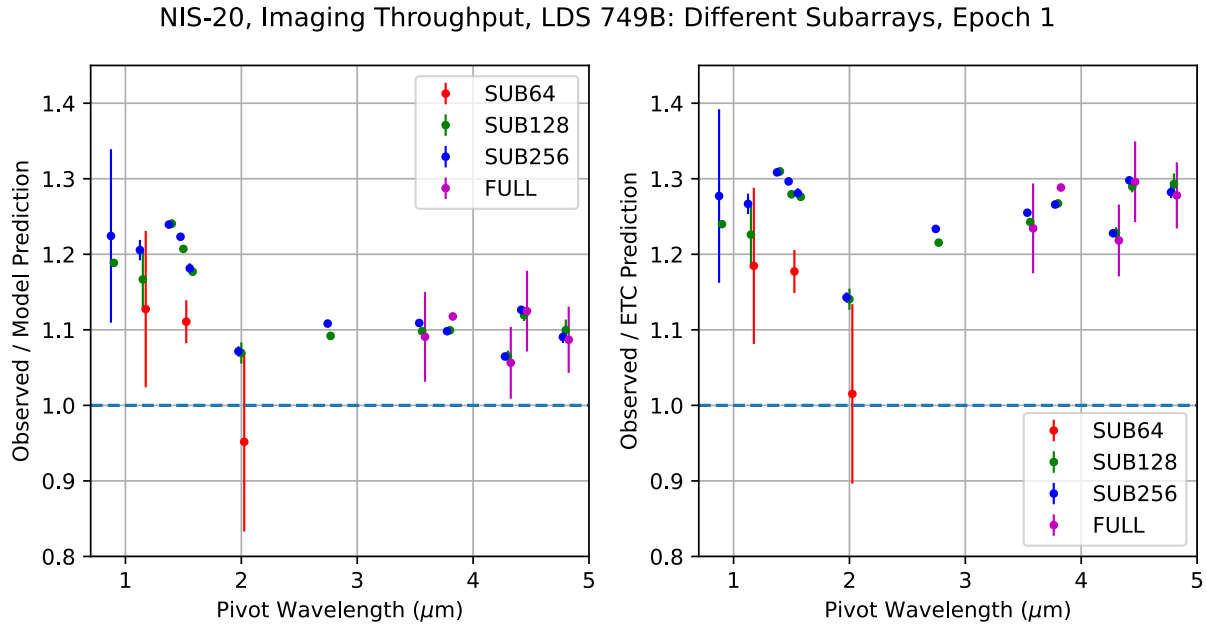

Figure 4: Integrated-light photometry of LDS 749B with all NIRISS filters taken with different subarrays. *Left Panel*: ratio of observed flux over NIRISS model prediction. *Right Panel*: ratio of observed flux over ETC prediction. Data are from the first epoch (Observation 1). See legend for symbols. The filter pivot wavelengths for the data points of the different subarrays have been offset slightly from one another to improve visibility.

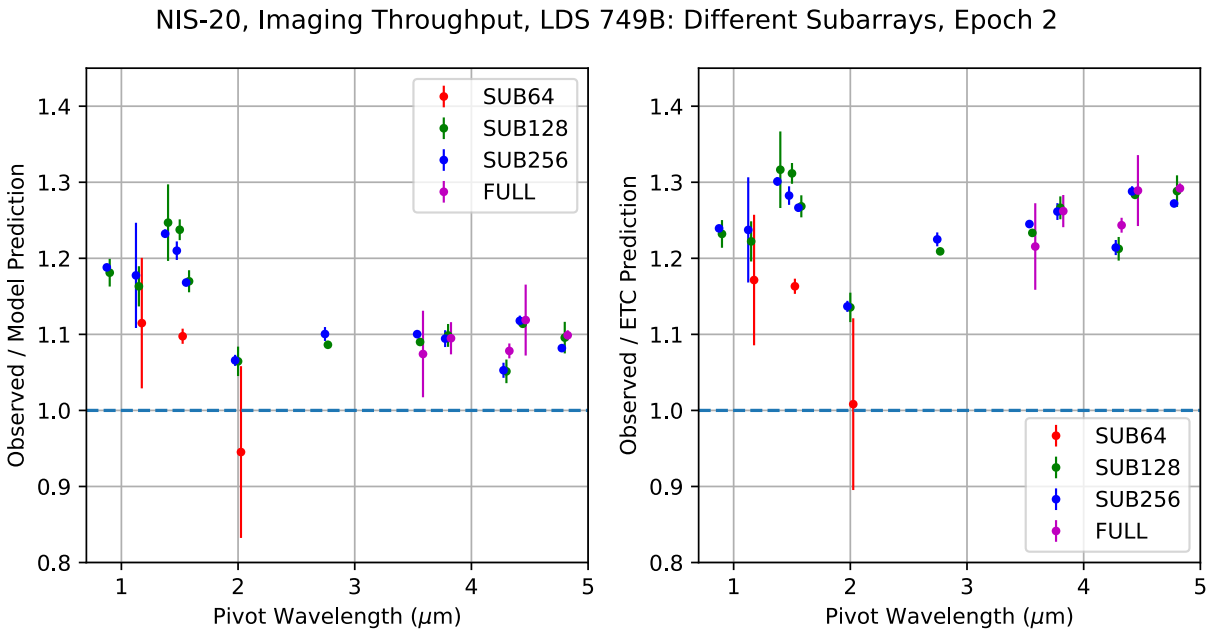

Figure 5: Same as Figure 4, but now for the second epoch (Observation 3).

4.2 Repeatability of Photometric Measurements

All exposures taken as part of Observations 1 and 2 were re-observed 16 days later (as Observations 3 and 4, respectively; see Table 1) in order to check the repeatability of the integrated-light photometry. For this purpose we calculate count rates for the LDS 749B data that are inverse-variance-weighted averages of the measurements in the subarrays SUB128, SUB256, and FULL (the latter only for the filters with which full-frame data were taken), using function `pgtools.weightav`. In Figure 6, we show the results for the two epochs. It can be seen that the throughput values are systematically somewhat smaller for epoch 2 than for epoch 1. The overall weighted mean ratio from all 12 filters is 1.006 ± 0.003, a marginal (2σ) deviation from unity. Further investigation of this difference suggests that it is due to changes of the primary mirror segment alignment during the period in between the two epochs. Specifically, there was a so-called "tilt event" of one of JWST's mirror segments due to a micrometeorite impact during this period, which was corrected as well as possible by the OTE team, but they were not able to completely correct the segment's position to the mirror alignment situation before the event (see Rigby et al. 2022). This is consistent with the changes we see in the EE curves between epoch 1 and epoch 2, as depicted in Figure 7. Specifically, the EE values are systematically somewhat higher for epoch 1 than for epoch 2. This is especially the case for the inner radii in the measurements of the filters with pivot wavelengths < 2 μm, for which the PSFs are the most undersampled by the NIRISS detector so that a relatively narrow PSF has the most significant impact on the inner EE values. Since the aperture corrections were derived using pre-launch WebbPSF models (because such models weren't yet available for on-orbit conditions), it seems likely that the main reason for the apparent decrease in throughput from epoch 1 to epoch 2 is due to a change in the PSF properties (and hence a change in the aperture correction) rather than an actual change in throughput. This assumption will be tested during Cycle 1 calibration.

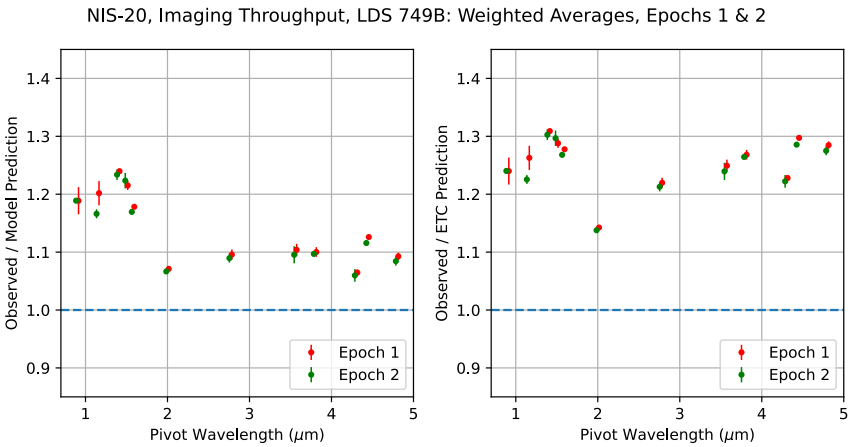

Figure 6: Similar to Figure 4, but now the different symbol colors indicate the results for the two different observing epochs. The data points in this figure represent count rates that are weighted averages of the results for subarrays SUB128. SUB256, and FULL.

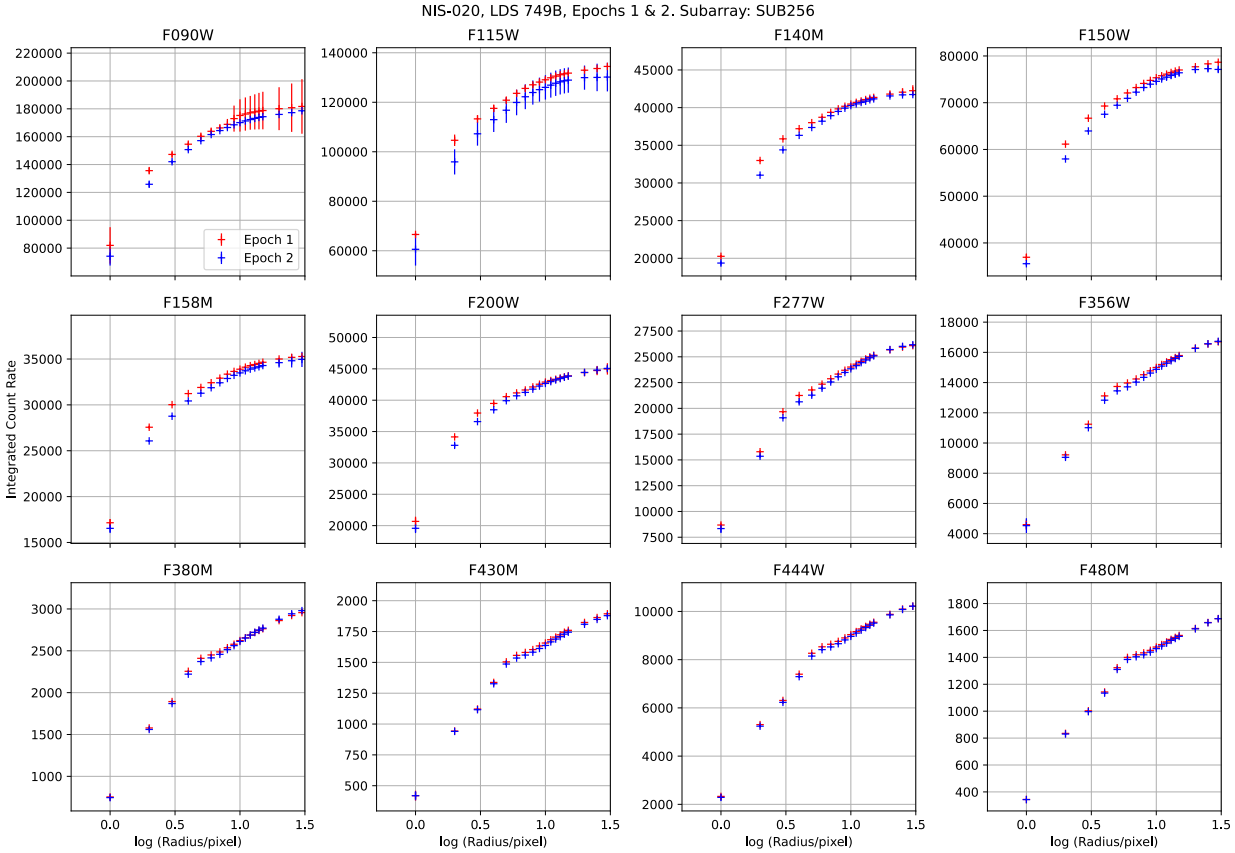

Figure 7: multi-aperture photometry for all NIRISS filters as derived from the SUB256 observations of LDS 749B during the two observing epochs. Red and blue symbols represent epochs 1 and 2 (or Observations 1 and 3), respectively. Filter names are indicated at the top of each panel. Note the slightly higher integrated count rate values for epoch 1, especially for the inner radii for filters with short pivot wavelengths (for which the PSFs are strongly undersampled by the detector).

4.3 Comparison with Pre-Launch Predictions

One of the things that stand out immediately when looking at Figures 4-6 is that the observed count rates are significantly higher than those predicted from the pre-launch throughput reference files. The observed count rates are higher by ~ 8 – 25% than those predicted by the "NIRISS throughput model", and by ~ 13–31% than the ETC predictions (see, e.g., Figure 6). Further analysis shows that the positive changes in the count rate are mainly due to the following effects:

1. A change in the OTE throughput (differences stay within 3% for NIRISS);
2. An increase in the throughput of the optics internal to NIRISS. This increase is significant at wavelengths < 2 μm;
3. A small overall renormalization of the quantum efficiency of the NIRISS detector;
4. Percent-level changes to the individual filter response curves in order to make the predictions match the observed throughput results.

Details about these changes and the resulting updates to the ETC Reference Files for NIRISS for the Call for Proposals of JWST Cycle 2 are described in a separate report (Volk et al. 2022b).

4.4 Comparing Imaging Throughputs as Measured using LDS 749B vs. P330-E

Figure 8 shows the imaging throughput in terms of the count rate ratio "observed / ETC prediction" as derived from the CLEARP photometry of flux standard stars LDS 749B and P330-E. The throughputs are consistent with each other to within 1σ, which lends credence to both the suitability of these stars as flux standards and the measurement accuracy. Furthermore, note that P330-E is a factor of ~30 brighter than LDS 749B at these wavelengths, suggesting that any count-rate-dependent non-linearity of the NIRISS detector stays within the measurement uncertainties of up to a few percent.

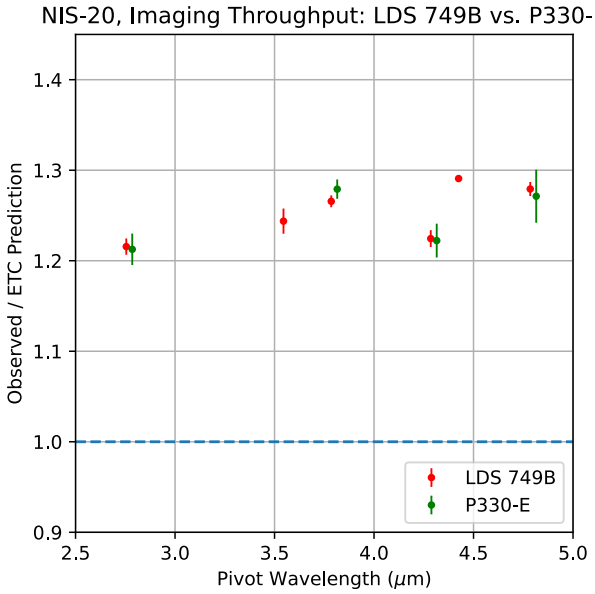

Figure 8: Observed / ETC prediction count rate ratio as function of filter pivot wavelength for the direct imaging measurements of LDS 749B and P330-E. For both stars, the data points reflect the average count rate of the two observing epochs. The filter pivot wavelengths for the data points of the different stars have been offset slightly from one another to improve visibility.

4.5 NRM/CLEARP Throughput Ratio

Measurements of P330-E were made both with the CLEARP and NRM elements in the pupil wheel, using filters F380M, F430M, and F480M, for the purpose of checking the NRM/CLEARP throughput ratio. The pre-launch predictions for the throughputs of the CLEARP and NRM elements were 0.84 and 0.15, respectively, corresponding to an NRM/CLEARP throughput ratio of 0.178. Observed ratios from the integrated-light photometry turn out to be marginally consistent with the prediction, as shown in Figure 9. Quantitatively, the overall weighted average ratio from the measurements is 0.175 ± 0.001, i.e., 3σ below the prediction. We did not update the pre-launch predictions of the throughputs of CLEARP and NRM based on this finding. More observations will be taken during Cycle 1 calibration programs which are expected to provide more precise measurements of the NRM/CLEARP throughput ratio.

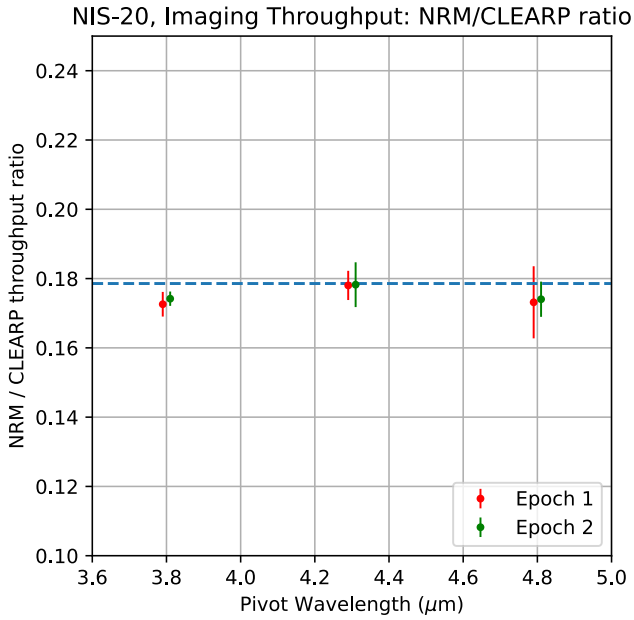

Figure 9: NRM / CLEARP throughput ratio as measured from data on P330-E in Observations 2 and 4. The horizontal dashed line at a ratio of 0.178 indicates the throughput ratio from pre-launch predictions, corresponding to a NRM throughput of 0.15 and a CLEARP throughput of 0.84. The filter pivot wavelengths for the data points of the different epochs have been offset slightly from one another to improve visibility.

5 Cross-comparison with Count Rate Measurements of K. Volk

We compare our results with those of K. Volk who used independent measurement methods to measure integrated-light imaging photometry for a variety of NIRISS commissioning programs including NIS-20 (see Volk et al. 2022a). Figure 10 depicts this comparison for the case of the exposures of LDS 749B taken during Observation 1 (see Table 1), using weighted average values from subarrays SUB128, SUB256, and FULL, as described in §4.2. All measured count rates are again divided by the ones predicted by the pre-launch ETC for this comparison. Note that the results from the two independent measurement methods are consistent to within 1σ, thus providing confidence in the throughput results.

6 Reference File Creation

The photometry results from commissioning program NIS-20 were used to create the imaging-related entries of the first PHOTOM pipeline reference file in CRDS from in-flight data. For imaging, this reference file is used to convert count rates in flat-fielded data for each imaging filter to surface brightness values in MJy/sr (see Volk et al. 2022a for details).
A description of the creation procedure for this file along with the associated Python scripts and other relevant files is available in the NIRISS GitLab area on the PHOTOM reference file, and will not be repeated here.

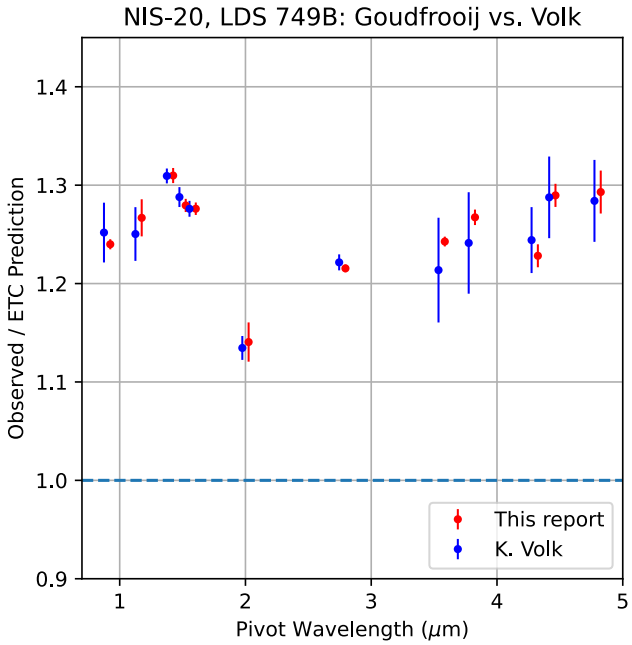

Figure 10: Observed / ETC Prediction ratio for the integrated photometry measurements of LDS 749B in this report versus those measured independently by K. Volk (see Volk et al. 2022a). The data points in this figure represent count rates that are weighted averages of the results for subarrays SUB128, SUB256, and FULL.

7 Summary

We presented the data reduction and analysis of commissioning program NIS-20 on NIRISS imaging throughput from two epochs of data (taken about 2 weeks apart), using a method using multi-aperture photometry of multiple dithered images. The method includes corrections to eliminate or minimize the effects of bad pixels and pixels with negative sky values in images with very short integration times. Aperture corrections were derived using WebbPSF images for which the PSFs were centered on the same sub-pixel positions as the actual stars in the (often strongly undersampled) NIRISS images. The main results of this program were:

1. The results revealed imaging throughputs that were between 12% and 31% **higher** than those predicted by the JWST Exposure Time Calculator (ETC), and between 7% and 24% higher than those predicted by the in-house "NIRISS model" based on the same ETC reference files. These results are being used to update the NIRISS ETC reference files for the Cycle 2 Call for Proposals.

2. The data revealed a problem with the frame read time of NIRISS subarrays with 64x64 pixels that were assumed in pre-launch operations. This problem was understood and subsequently corrected in PRDOPSSOC-054 as well as the relevant NIRISS OSS script.
3. The measurements of the second epoch's data revealed throughputs that were about a percent lower than the first epoch. This difference is tentatively attributed to changes in the PSF (i.e., changes in the optical path differences between the mirror segments) rather than to actual throughput differences with time.

Further imaging throughput observations in future calibration observations during regular JWST operations will be used to monitor and/or update the results described in this report.

8 References

Bohlin, R. C., & Koester, D., 2008, "The Absolute Flux Distribution of LDS 749B", The Astronomical Journal, 135, 1092

Bohlin, R. C., & Landolt, A. U., 2015, "The CALSPEC Stars P177D and P330E", The Astronomical Journal, 149, 122

Gordon, K. D., et al., 2022, "The James Webb Space Telescope Absolute Flux Calibration. I. Program Design and Calibrator Stars", The Astronomical Journal, 163, 267

Goudfrooij, P., 2022, "Accuracy and Precision of Centroid Algorithms in the `photutils` Python package for NIRISS Point Spread Functions", JWST Technical Report JWST-STScI-008116, SM-12

Goudfrooij, P., & Cox, C., 2018, "The Pre-Flight SI Aperture File, Part 5: NIRISS", JWST Technical Report JWST-STScI-006317, SM-12

McCullough, P. R., Regan, M., Bergeron, L., & Lindsay, K., 2008, "Quantum Efficiency and Quantum Yield of an HgCdTe Infrared Sensor Array", PASP, 120, 759

Perrin, M., et al., 2012, "Simulating Point Spread Functions for the James Webb Space Telescope with WebbPSF", Proc. SPIE, Vol. 8442, article id. 84423D

Perrin, M., et al., 2014, "Updated Point Spread Function Simulations for JWST with WebbPSF", Proc. SPIE, Vol. 9143, article id. 91433X

Pontoppidan, K., Pickering, T., & Laidler, V., 2015, "Overview of the JWST ETC Reference Files", JWST Technical Report JWST-STScI-004257, SM-12

Rigby, J., Perrin, M., McElwain, M., et al., 2022, "Characterization of JWST science performance from commissioning", NASA/ESA/CSA White Paper at this URL

Volk, K., et al., 2022a, "NIRISS Imaging Photometric Observations in Commissioning", JWST Technical Report JWST-STScI-008269, SM-12

Volk, K., et al., 2022b, "NIRISS On-Orbit Throughput Calibration", JWST Technical Report JWST-STScI-008268, SM-12